Journal of Power Sources 644 (2025) 237129

Contents lists available at ScienceDirect

Journal of Power Sources

journal homepage: www.elsevier.com/locate/jpowsour

Ultrafast activation to form through-hole carbon facilitates ion transport for high specific capacity supercapacitors

Hongxia Gao [a], Yikun Li [a], Xueyan Wu [a,*], Yan Lv [a], Chunmei Ma [b], Yanchun Pei [a], Na Liang [a], Fanze Meng [a], Pengfei Dong [a], Jixi Guo [a,**]

[a] *State Key Laboratory of Chemistry and Utilization of Carbon Based Energy Resources, College of Chemistry, Xinjiang University, Urumqi, 830017, Xinjiang, PR China*
[b] *Xinjiang Xuandong Energy Co., Ltd., Hami, Xinjiang, 963000, PR China*

HIGHLIGHTS

- Activated carbon is prepared via flash Joule heating within 20 s.
- Through-hole structure and heteroatom doping improve electrochemical performance.
- The symmetric device reveals high energy density and good electrochemical stability.

ARTICLE INFO

Keywords:
Supercapacitor
Flash joule heating
Activated carbon
Heteroatom doping

ABSTRACT

The pore structure is the critical parameter affecting the performance of activated carbon (AC) based supercapacitors. However, most conventional high-temperature thermal treatment of AC is time-consuming, energetically demanding, and easy destroyed of pore structure. Here, the AC with through-hole structure is prepared by flash Joule heating method within 20 s, shortens the transport distance of electrolyte ions, solves the problem of slowing down the electro-adsorption kinetics with large specific surface area (1039 $m^2\ g^{-1}$). In addition, the rapid activation process helps to prevent the etching of heteroatoms by the KOH, so that the content of heteroatom is higher than tube furnace, and the pseudocapacitance is increased. Based on these, electrode material exhibits high specific capacitance of 313.7 F g^{-1} at 1 A g^{-1}. Symmetrical supercapacitor reveals specific capacitance retention of 99.8 % after 10000 circles in 6 M KOH. The prepared AC is assembled into a button cell by using 1 M TEATFB/AN electrolyte, it delivers good energy density of 57.8 Wh kg^{-1} at the power density of 748.5 W kg^{-1}, and a wide voltage window of 3 V. This strategy offers a broad prospect for rapid preparation of carbon-based electrode materials.

1. Introduction

The consumption of fossil fuels on a global scale has resulted in a number of natural disasters., so the continuous development and application of new energy technologies is particularly significant [1–3]. Supercapacitors (SCs) occupy a critical position in electrochemistry due to their long cycle stability, which are widely used in green energy storage devices [4,5]. Base on the different reaction mechanism, SCs are classified into electric double-layer supercapacitors (EDLCs) and pseudocapacitors (PCs) [6]. Carbon materials are frequently employed as electrode materials, which including AC [7], graphenes [8], carbon nanofibers [9] and carbon nanotubes. AC is widely used in supercapacitors because of its large SSA and good electrical conductivity. The properties of activated carbon-based supercapacitors are closely related to the pore structure. The micropores (<2 nm) make the carbon material to have a larger SSA and provide more active sites for electrochemical energy storage, ultra-micropore (<0.7 nm) can effectively reduce the thickness of the EDLCs and increase the specific capacitance significantly, mesoporous pores (2–50 nm) facilitate the transport of ions, large pores (>50 nm) are conducive to electrolyte storage. However, with the increase of the SSA, ions in the electrolyte are more easily adsorbed on the surface of the micropores, resulting in greater resistance

---

* Corresponding author.
** Corresponding author.
E-mail addresses: Wuxy90@xju.edu.cn (X. Wu), jxguo1012@163.com (J. Guo).

https://doi.org/10.1016/j.jpowsour.2025.237129
Received 24 December 2024; Received in revised form 19 March 2025; Accepted 18 April 2025

to ion transport and movement, and the energy density and power density are also decreased. Therefore, the construction of through-hole, and the formation of interconnected through-hole network can promote the migration and transport of ions in solution, reduce the resistance of ion current flow, and improve the electrochemical performance of electrode materials. The interconnected channels between micropores, mesoporous and macropores providing facile pathways for electrolyte movement [10,11].

Although EDLCs have excellent cycle stability, their specific capacitance is lower than PCs. Therefore, doping heteroatoms in the carbon skeleton to increase the pseudocapacitance is considered as a promising method to improve the specific capacitance. In addition, the rich porous structure will disrupt the conductive network of the carbon material, resulting in a decrease in conductivity, while heteroatom doping can enhance the conductivity of the electrode material in addition to improving the pseudocapacitance. Zhao et al. [12] synthesized MXene/carbon nanotube electrodes with vertically aligned channels using a directional freezing strategy, reducing interfacial resistance, so that the assembled device provides a specific capacitance of 231 F g^{-1} and a maximum energy density of 10.17 Wh kg^{-1} at 2 mV s^{-1}. Yang et al. [13] prepared biochar with controllable micro/mesoporous structure by adjusting the ratio of salt to chitin and increasing the total nitrogen content and SSA (>1000 m^2 g^{-1}), the pseudocapacitance can be increased by the N content to achieve a specific capacitance of 301.2 F g^{-1}.

AC based electrode materials usually need to be heat treated in an inert atmosphere, and carbon materials are etched with activators to improve the pore structure, which usually requires mixing more than two activators and consuming more than three times the mass of the carbon precursor [14]. The traditional heat treatment is usually carried out via thermal radiation, convection, or conduction, and the heating rate is less than 10 K min^{-1}. Therefore, the high-temperature treatment and activation process of AC often takes several hours to complete, and longer heating times can lead to the following problems: The carbon precursor will continuously react with the activator during the heating process. With the reaction, the pore diameter will continue to grow, the structure of the ultra-micropores will be destroyed and the yield of AC will be reduced. When the activator etched carbon, it also etched heteroatoms in the carbon material. [15,16]. FJH is a method of heating through high temperature radiant heat shock, which can complete the activation and carbonization process of AC in a few seconds. The use of its rapid heating and cooling characteristics can prevent further destruction of the pore structure during the heat treatment process, as well as avoid additional etching of N and O atoms by the activator. However, there are few reports on this aspect.

Coal-based carbon materials contain a large number of aromatic compounds, but the high resistance and poor wettability hinder their further application. The introduction of heteroatoms into the carbon lattice, resulting in the changes of surface functional groups and structures, can improving this problem [17]. In order to improve the chemisorption of ions on carbon electrode material, Roy [18] et al. introduced N into the carbon material to reduce the electrode/electrolyte interface resistance, improve the hydrophilicity, and show excellent electrochemical performance. Dong [19] et al. show that O-doped carbon surfaces exhibit an increase in dipole moments, suggesting a rise in surface polarization. O functional groups on the surface of carbon materials has been shown to improve the ability to adsorb electrolyte ions (K^+). In addition, the O-doped surface experiences a significant increase in adsorption energy, thus enhancing the pseudocapacitance of the supercapacitor. Pan [20] et al. prepared N/O co-doped carbon materials. The density functional theory (DFT) shows that N/O doping can produce heterogeneous atomic charge distribution, which can enhance the surface polarity and thus improve the surface wettability to the electrolyte. In conclusion, the coal is treated with HNO_3 and H_2SO_4, the aromatic compounds in the coal are transformed into nitro aromatics through nitration reaction, N atom is introduced. A large number of carboxyl groups and oxygen-containing functional groups are introduced into the side chain and edge of the aromatic ring through oxidation reaction. The successful doping of N/O improves the electrochemical properties of carbon electrode materials.

Due to the rapid heating and cooling characteristics of flash Joule heating, the uniform mixing of carbon precursors and activators becomes important. Therefore, oxidized coal is used as the precursor, the surface of oxidized coal contains a large number of acidic oxygen-containing functional groups such as phenolic hydroxyl group and -COOH. KOH as an alkaline activator neutralizes the acidic functional group before the activation process, which can make the activator fully contact with oxidized coal and prevent resource waste and uneven pore structure. In the activation process, functional groups such as -OH help to increase the active site, and KOH is etched from the surface to the inside of the carbon material, which can form a through-hole structure by adjusting the ratio [21]. K^+ further corrodes the carbon layer and forms pores. Stable functional groups such as C-O-C and C=O are formed by the reaction of -COOH and -OH on the surface of oxidized coal, and CO_2 and H_2O are released at the same time [22].

In this work, the coal is pre-oxidized to enrich its surface with heteroatoms and oxygen-containing functional groups. KOH is used as activator, coal-based AC with a SSA of 1039 m^2 g^{-1} was quickly prepared by flash Joule heating. The through-hole network from micropores to macropores shortened the distance of ion diffusion, two different heat treatment methods of Joule heating and tube furnace were used to investigate their differences in structure, composition and electrochemical properties. In addition to the advantages of the porous structure of the Joule-heated sample, the faster reaction process also prevents excessive etching of heteroatoms, the sample has a higher O content (24.18 %) and N content (3.32 %) compared to the tube furnace. Base on the advantages of pore structure and composition, Joule-heated sample has demonstrated a specific capacity 313.7 F g^{-1} at 1 A g^{-1}, it delivers energy density of 57.8 Wh kg^{-1} (power density 748.5 W kg^{-1}) in 1 M TEATFB/AN (Tetraethylammonium tetrafluoroborate/acetonitrile).

2. Experimental section

2.1. Preparation of oxidized coal

The preparation of oxidized coal (OC) originated from our group's previous work [23,24]. 10 g coal is mixed with 180 mL H_2SO_4 and 60 mL HNO_3 in a beaker and stirred for 12 h. The acidified coal is washed three times with deionized water, named the product as OC.

2.2. Fabrication of TF-AC and FJH-AC-X

0.2 g OC and 0.2 g KOH were ground in mortar until fully grind, and the mixture was heated to 1000 °C in a tube furnace and held for 2 h, the heating rate is 5 K min^{-1}. The sample with 1 M HCl followed by repeated centrifugation with distilled water and was named TF-AC.

The mixture of 0.2 g OC and different masses of KOH (0.1, 0.2, 0.3 g) was fully ground and evenly mixed. The voltage and current of Joule heating are 40 V and 300 A respectively, heating rate 200 °C/s, set temperature 1000 °C. The subsequent washing method is the same as TF-AC. Coal-based porous carbon designated as FJH-AC-X. (In this article, TF represents the sample treated in the tube furnace, AC represents activated carbon, FJH represents samples treated with flash Joule heating, X is the mass ratio of OC to KOH. X = 1 means m_{OC}: m_{KOH} = 1:0.5, X = 2 means m_{OC}: m_{KOH} = 1:1, X = 3 means m_{OC}: m_{KOH} = 1:1.5)

3. Results and discussion

The manufacturing process of FJH-AC-2 is illustrated in Scheme 1. Heteroatoms and the multitudinous of functional groups directly affect the conductivity and wettability of supercapacitors, which are crucial to

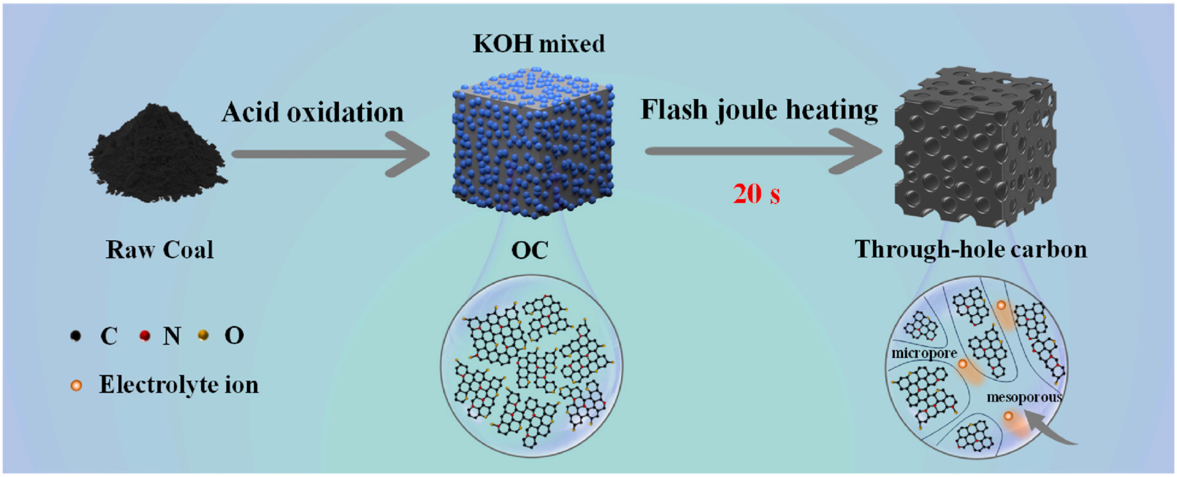

Scheme 1. Formation Schematic of FJH-AC-2.

the performance of supercapacitors [25–27]. Therefore, N, O atoms and oxygen-containing functional group were successfully introduced into the carbon skeleton and macromolecular structure side chain of carbon by being treated with mixed acid. Flash Joule heating, which can be heated at a rate of 200 K s^{-1} (Fig. S1.), KOH will rapidly react with OC to form a unique structure [28,29]. After reaching the set temperature the heating ceased and rapid cooling ensued, the rapid cooling process preserving these specific morphologies. However, in the tube furnace, KOH melts slowly and due to prolonged heating time, the reaction proceeds towards a reduction in Gibbs free energy, causing small droplets to gradually coalesce into larger ones and form large and uneven pores [28]. In a tube furnace, the long-term heating treatment causes more carbon in OC to be etched by KOH, and the small molecule compounds components in OC will also be thermal decomposed more completely. Hence these two reasons lead to the AC obtained by carbonization in tube furnace is less than that obtained by joule heating treatment, the yield of FJH-AC-2 is as high as 71.3 %, while the yield of TF-AC is only 33.9 % (Fig. S2).

As shown in Fig. 1b and S3, the TF-AC produced by the tube furnace has a relatively rough surface, with its 3D structure destroyed and no specific shape is formed. Fig. 1 a and 1 c demonstrate that FJH-AC-1 is composed of numerous granules. The KOH melts and disperses into smaller droplets, which can etch the OC and form a granular morphology. As shown in Fig. 1b–d, with the increase in the proportion of KOH, the KOH drops size becomes larger, resulting in an increase in the porous size formed, this leads to the formation of through-hole structures for FJH-AC-2 (Fig. S4 and S5.). As the ratio of KOH continues to increase, the pore size of FJH-AC-3 also increased, however, the through-hole structure is partially destroyed (Fig. 1a and e). These different morphologies are related to the variations in heating rate and KOH ratio. The morphology of FJH-AC-2 was further characterized using TEM. The presence of small mesoporous and micropores is observed in (Fig. 1f), FJH-AC-2 does not exhibit obvious carbon lattice fringes, indicating its existence in the form of amorphous carbon. Elements C, O and N are distributed within FJH-AC-2 (Fig. 1g), the structure of interconnected macropores can be observed, which facilitates ion transport in electrolyte.

Fig. 2a reveals the XRD spectroscopy of TF-AC and FJH-AC-X. Two broad peaks appeared in the vicinity of 23° and 44°, corresponding to the (002) and (100) crystal planes of carbon materials [30]. The wide and flat shape of the two characteristic peaks indicates high degree of defects [31,32], FJH-AC-X and TF-AC has a relatively high porosity. As shown in Fig. 2b, there are two characteristic peaks at about 1350 cm^{-1} and 1580 cm^{-1}, representing the D and G bands of carbon materials. The strength of the D-band indicates the degree of defects, while the strength of the G-band indicates its degree of graphitization. The I_D/I_G values of TF-AC, FJH-AC-1, FJH-AC-2 and FJH-AC-3 are 1.24, 0.82, 0.83, and 0.99. The value increases with the increase of activation time and KOH ratio. The higher I_D/I_G of carbon materials suggests greater pore abundant [33,34].

To gain further insight into the pore structure, the N_2 adsorption-desorption isotherms and PSD data for TF-AC and FJH-AC-X are presented in Fig. 2c and Fig. S6, respectively. All samples are exhibit composite curves of type I and type IV, with the curve sharply rising at low relative pressure ($P/P_0 < 0.1$), indicating a significant presence of micropores [35,36]. At high relative pressure ($0.4 < P/P_0 < 1$), mesoporous is proven by the obvious hysteresis loops observed in the curve, in addition, the TF-AC hysteresis loop belongs to the type of H3, which represents the generation of slit pores, and the FJH-AC-2 belongs to the type of H4, which represents the generation of interstice pores. Interstice pores generally a collection of spherical pores and straight cylindrical pores, this matches with the pore types of the through holes observed by SEM and TEM. [37–39]. As shown in Table S1, the SSAs of TF-AC and FJH-AC-2 are 1313 and 1039 $m^2\ g^{-1}$, respectively. Even though TF-AC has a larger SSA, the larger SSA makes it easier for ion to be adsorbed on the micropores, which slows down the ion migration and increases the electrical resistance and thus reduces the electrochemical performance. Compared with the smooth surface of TF-AC, FJH-AC-2 has more through-hole structures, which are favorable for ion transport, and enhancing the electrochemical performance [11]. The increase in the SSA is due to a longer reaction time between KOH and OC in the tube furnace. The PSD reveals that FJH-AC-2 has a higher content of ultra-micropores (<0.7 nm), and the it matches more closely with the size of solvated ions, that is, hydrated K^+ ions (0.63 nm) and OH^- (0.6 nm), thus improving the electrochemical performance [40,41]. The diagram of desolvation of hydrated ions depicted in in Fig. 2d, the ions in the aqueous electrolyte combine with water to form solvated ions. When a voltage is applied to the electrode material, these solvated ions will slightly deform in pores smaller than their size and lose some water molecules. This desolvation phenomenon reduces the thickness of the double electric layer, thereby reducing the distance between the central ion and electrode surface and significantly improving its electrochemical performance [42]. Under the same KOH ratio, FJH-AC-2 have a large number of ultra-micropores due to its rapid activation. However, the reaction time between TF-AC and activator is prolonged, resulting in a larger pore size and reduce the content of ultra-micropores, leading to performance deterioration. FJH-AC-2 is an ideal material for supercapacitors due to its reasonable distribution of micropores, mesoporous and macropores, which form an interconnected hierarchical pore structure.

As shown in Fig. S7 and Table S2, the changes of functional groups are explored through FTIR spectra. The infrared spectrum of OC and two

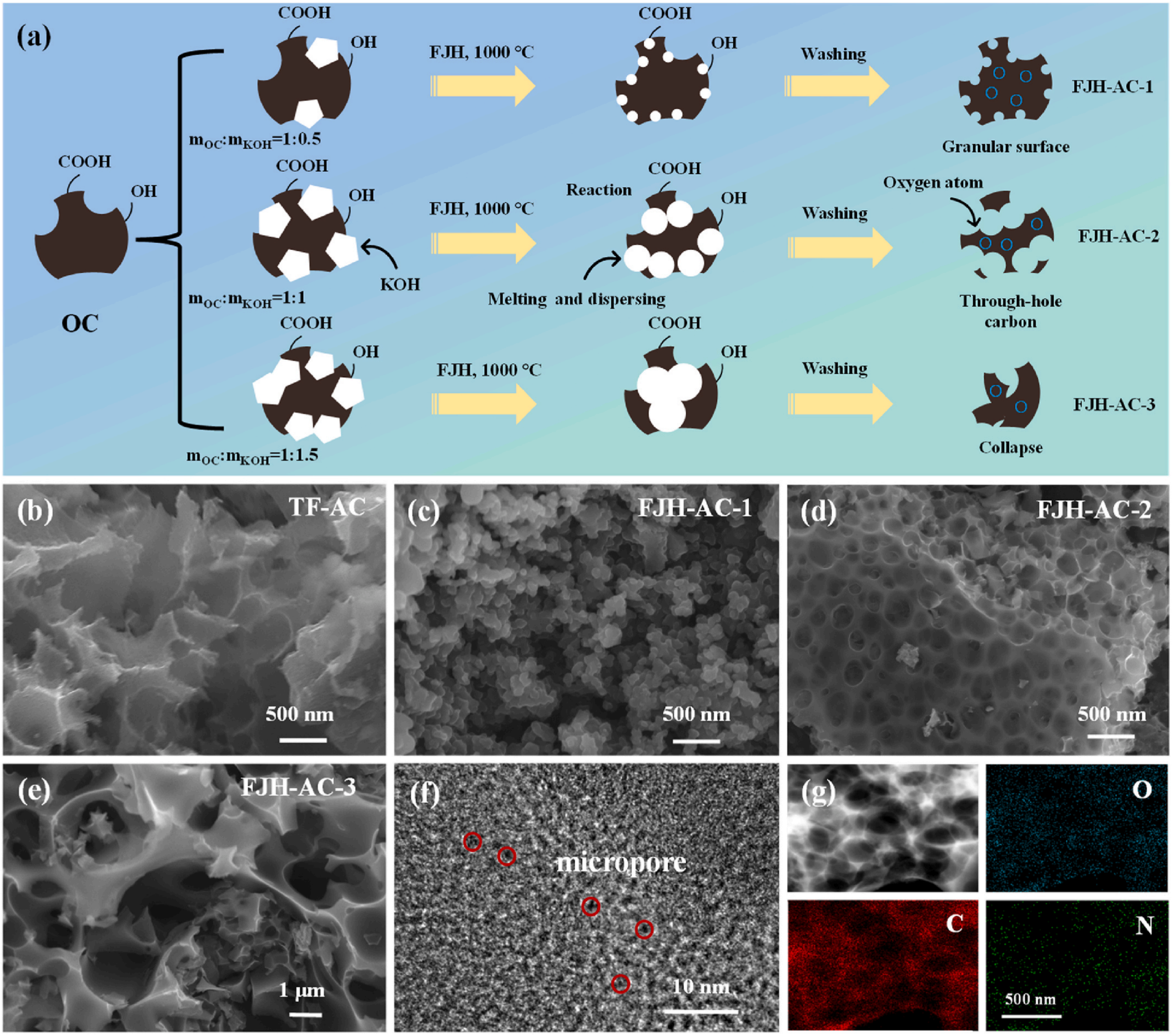

Fig. 1. (a) Mechanism of pore structure formation in flash Joule heating process with different KOH ratio. (b) SEM images of TF-AC; (c) FJH-AC-1; (d) FJH-AC-2; (e) FJH-AC-3. (f) TEM images of FJH-AC-2 and (g) element mapping of C, O and N.

samples with different heating methods. From the spectra, it can be observed that abundant functional groups, including -COOH, -NO_2, -C=O and -OH, are introduced to the surface of OC. The FJH-AC-2 contains significantly more functional groups than that of TF-AC, which is caused by the two factors of heating time and heating rate. The longer the heating time, the acidic functional groups in OC and KOH react more fully, resulting in a reduction of O-H bond and C=O of carboxyl functional groups at 3564 cm^{-1} and 1730 cm^{-1}. As a result, this functional groups basically disappears in TF-AC. On the other hand, the longer heating time make more complete etching of C atoms and heteroatoms by KOH, so the content of nitro functional groups and functional groups in the TF-AC is diminished.

Elemental composition and content of TF-AC and FJH-AC-2 were analyzed through XPS testing. The binding energies of TF-AC and FJH-AC-2 at 284.8, 400.1 and 530.1 eV correspond to the peaks of C1s, N1s and O1s. The C1s spectrum of FJH-AC-2 (Fig. 2f) was fitted to five peaks, which correspond to C-C, C-N, C-O, C=O, and O-C=C bonds located near 284.8, 286.2, 287.1, 289.1, and 291.1 eV respectively [43]. The N1s spectrum (Fig. 2g) was decomposed into four peaks that corresponded to N-5 (400.1 eV), N-6 (398.4 eV), N-Q (402.2 eV), and N-X (404.5 eV). N-5 and N-6 located in the marginal part of the carbon, which can improve the wettability and provide reaction active sites [44,45]. N-Q refers to quaternary nitrogen, and the N-Q group can alter the charge density that provide positive charge and enhance the conductivity [46,47]. The O1s spectrum was fitted by four peaks (Fig. 2h), centered at 531.6, 533.2, 535.3, 537.6 eV, which could be assigned to C=O, C-O, O=C-O-C=O, O=C-O [48]. The content of O in FJH-AC-2 is 24.18 %, which is beneficial to the wettability and increases the capacitance performance (Table S4). The total content of N, O and the richness of functional groups in FJH-AC-2 are much higher than those in TF-AC (Fig. S8, Table S3 and S5), indicating that the types of the heating method change the content of oxygen, nitrogen and functional groups when the sample proportion is kept constant. Longer heating times are not conducive to the retention of heteroatoms. Therefore, it can be predicted that FJH-AC-2 has more excellent electrochemical properties. The contact angle is a crucial tool to measure the surface wettability

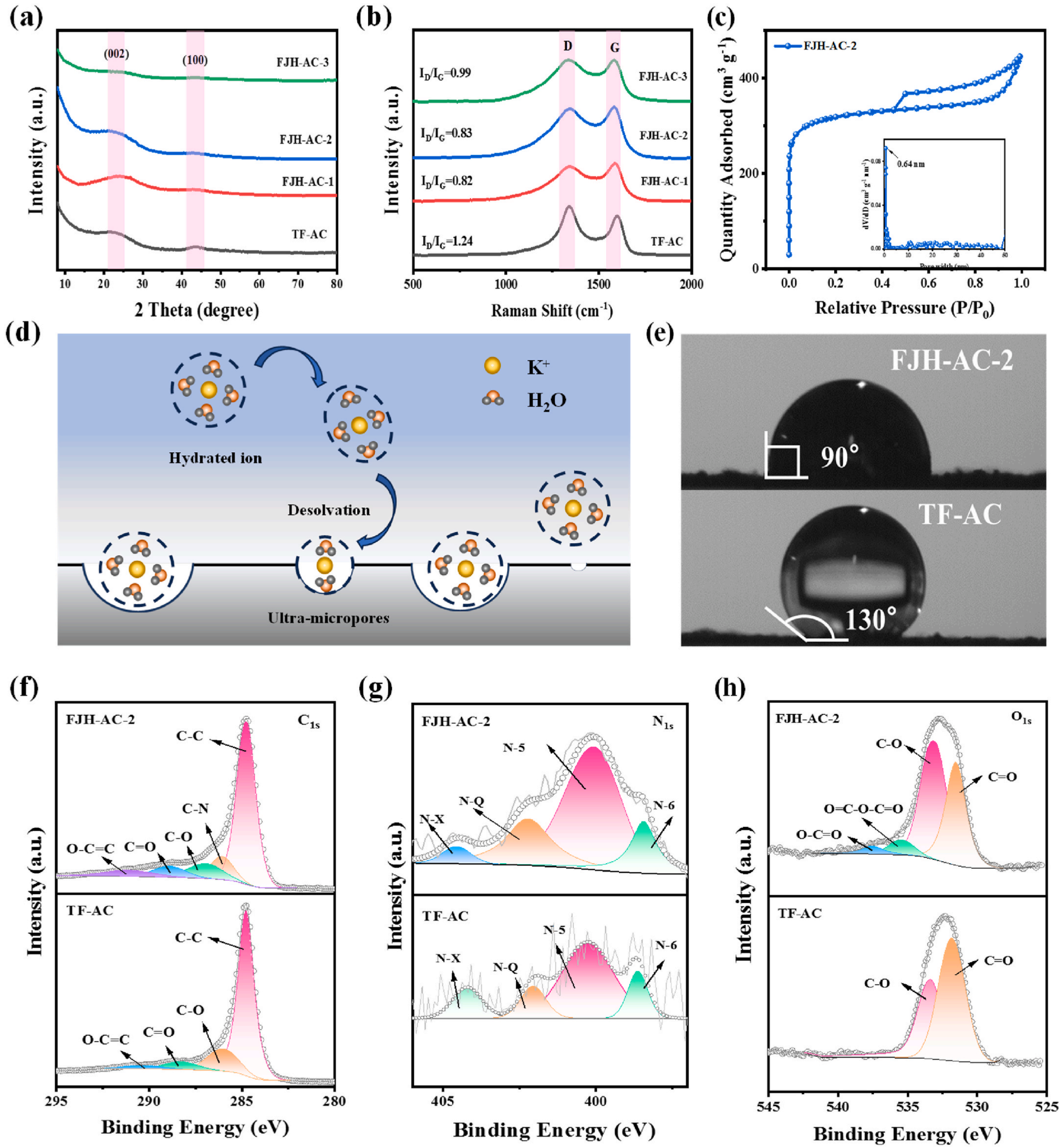

Fig. 2. (a) XRD patterns and (b) Raman spectra of TF-AC and FJH-AC-X. (c) N_2 adsorption-desorption isotherms and pore size distribution curves of FJH-AC-2. (d) Schematic diagram of desolvation of hydrated ions. (e) Water contact angels of TF-AC and FJH-AC-2. (f) C1s, (g) N1s, (h) O1s XPS spectra of TF-AC and FJH-AC-2.

(Fig. 2e). By comparing the water contact angles of TF-AC and FJH-AC-2, angles of TF-AC and FJH-AC-2 are 130° and 90° respectively, which indicates that FJH-AC-2 is more hydrophilic, which is caused by the fact that FJH-AC-2 contains more heteroatom and functional groups.

Electrochemical properties of TF-AC and FJH-AC-X were characterized using a three-electrode system, with 6 M KOH. In Fig. 3a, the GCD curves of TF-AC and FJH-AC-X exhibit approximately triangular shapes. The specific capacitance of TF-AC, FJH-AC-1, FJH-AC-2, and FJH-AC-3 can also be calculated as 140.8, 226.0, 313.7 and 247.7 F g^{-1} respectively. Among them, FJH-AC-2 exhibits excellent electrochemical performance (Table S6). Meanwhile, the CV curves of TF-AC and FJH-AC-X displayed in Fig. 3b exhibit an approximately rectangular shape. Both of the CV and GCD curves present the energy storage mechanism of the electrode is predominantly governed by the EDLCs behavior. It can be observed that FJH-AC-2 exhibits the highest specific capacitance because its higher heteroatom and functional groups, which lead to the

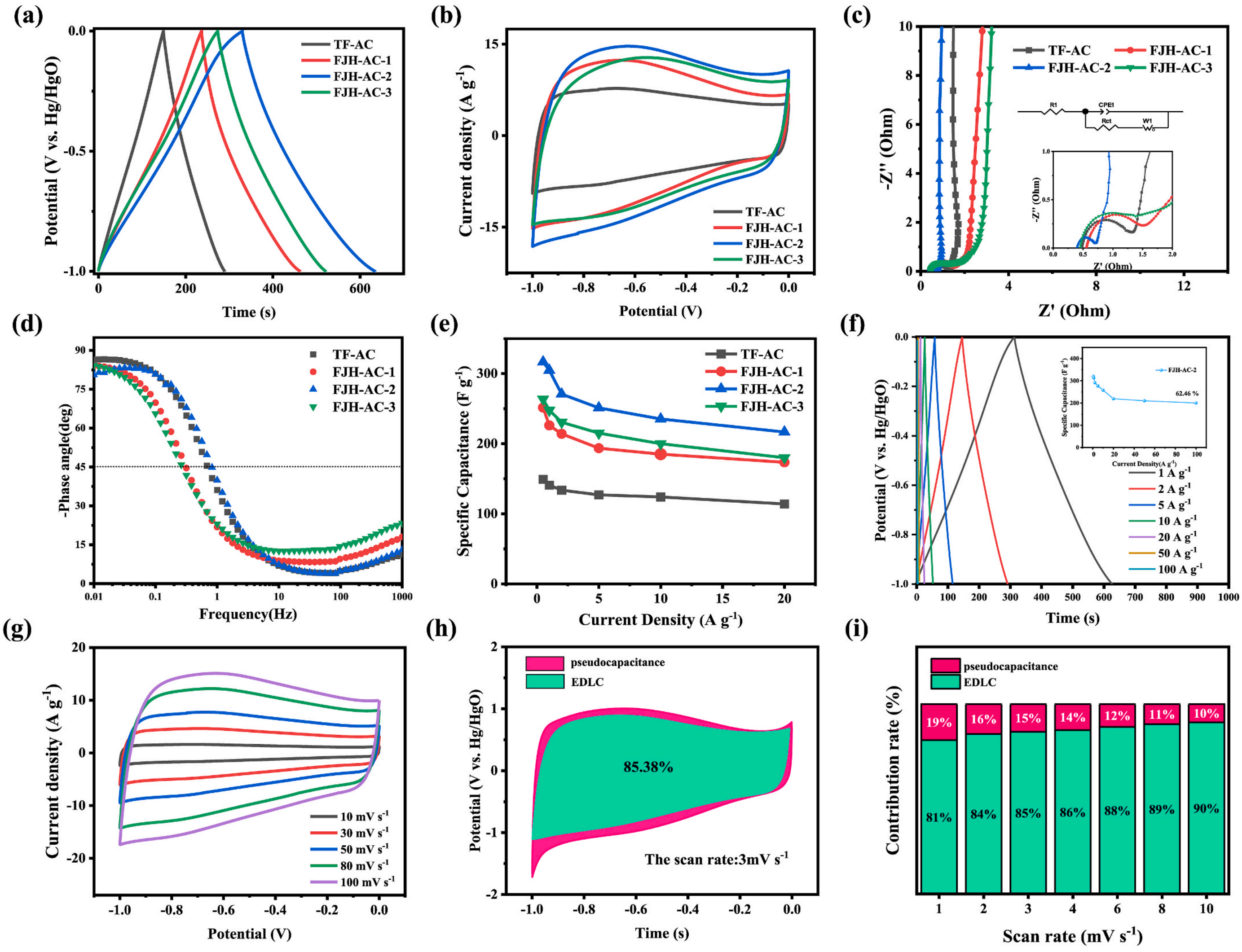

Fig. 3. Three-electrode electrochemical performance of TF-AC and FJH-AC-X: (a) GCD curves at current density of 1 A g^{-1} and (b) CV curves at scan rate of 50 mV s^{-1} of all sample; (c) Nyquist plots; (d) Bode plots of the samples; (e) rate performance of all samples; (f) GCD curves obtained at different current densities and (g) CV curves of FJH-AC-2 at different scan rates; (h) capacitance contribution at 3 mV s^{-1} and (i) capacitance contribution ratio at different scan rates of FJH-AC-2.

occurrence of pseudocapacitance electrochemical behavior [49–52]. Secondly, because the advantages of ultra-micropores and through-holes, the ultra-micropores match the size of hydrated ions in solution, and desolvation occurs to enhance the specific capacitance. Meanwhile the through-hole that connects the micropores and mesopores, which shortens the path of the ion migration, and then accelerates the transportation of the ions in solution, the electromobility rises, and the specific capacitance is increased [10,11]. Fig. 3c represents a Nyquist diagram for all samples, with Rs and Rct listed in Table S7. The Rs (0.42 Ω) and Rct (0.22 Ω) of FJH-AC-2 is the smallest, because the through-hole structure facilitates the transport of electrolyte ions [53–55]. From the Bode diagram in Fig. 3d shows that all samples are close to the phase angle of −90°, which means that the ideal capacitance characteristics for EDLCs. The relaxation time (τ_0) for TF-AC, FJH-AC-1, FJH-AC-2 and FJH-AC-3 are 1.46, 3.16, 1.21 and 3.83 s, respectively. The shorter relaxation time indicates a stronger ion transport ability of the electrode material, FJH-AC-2 has the smallest resistance and relaxation time [56,57]. The FJH-AC-2 exhibits good rate performance as a supercapacitors electrode material (Fig. 3e). The electrochemical performance of FJH-AC-2 is further analyzed. By examining the GCD diagram of different current densities (Fig. 3f) and CV diagram of different sweep speeds (Fig. 3g), as the scan rate and current density increase, the curves of FJH-AC-2 remains symmetrical without any obvious deformation, indicating that the material has remarkable chemical reversibility [58]. The specific capacitance changes from 320.5 to 200.2 F g^{-1} (0.5–100 A g^{-1}), and the capacitance retention possesses 62.5 %. The ratio of pseudocapacitance is analyzed in Fig. 6h, it can be observed that the percentage of double electric layer capacitance at 3 mV s^{-1} in the total capacitance is 85.38 %. At a sweep speed of 1 mV s^{-1}, the proportion of pseudocapacitance can reach 19 %. With the sweep speed continuous increase, some reactions may not have enough time to occur, therefore, the proportion of EDLC will correspondingly increase while the proportion of pseudocapacitance will decrease (Fig. 3i).

To further verify the application performance of TF-AC and FJH-AC-2 as electrode materials for supercapacitors, symmetric supercapacitors were assembled in three different electrolytes, and Fig. 4a shows the two-electrode system assembly diagram, FJH-AC-2 acts as both the positive and negative terminal, the through-hole of FJH-AC-2 provides a pathway for ion transport. From Fig. 4b and c, it can be observed that all samples have shapes similar to isosceles triangles and rectangles, this indicates that their energy storage mechanism is controlled by EDLCs. The electrochemical properties of TF-AC, FJH-AC-1, FJH-AC-2, and FJH-AC-3 were determined to be 30.1, 50.7, 107.8, and 83.7 F g^{-1}, respectively at 1 A g^{-1}. The FJH-AC-2 electrode exhibits the longest discharge time and the best electrochemical performance. The FJH-AC-2 exhibits a capacity retention rate of 70.8 % (Fig. S9), indicating satisfactory rate

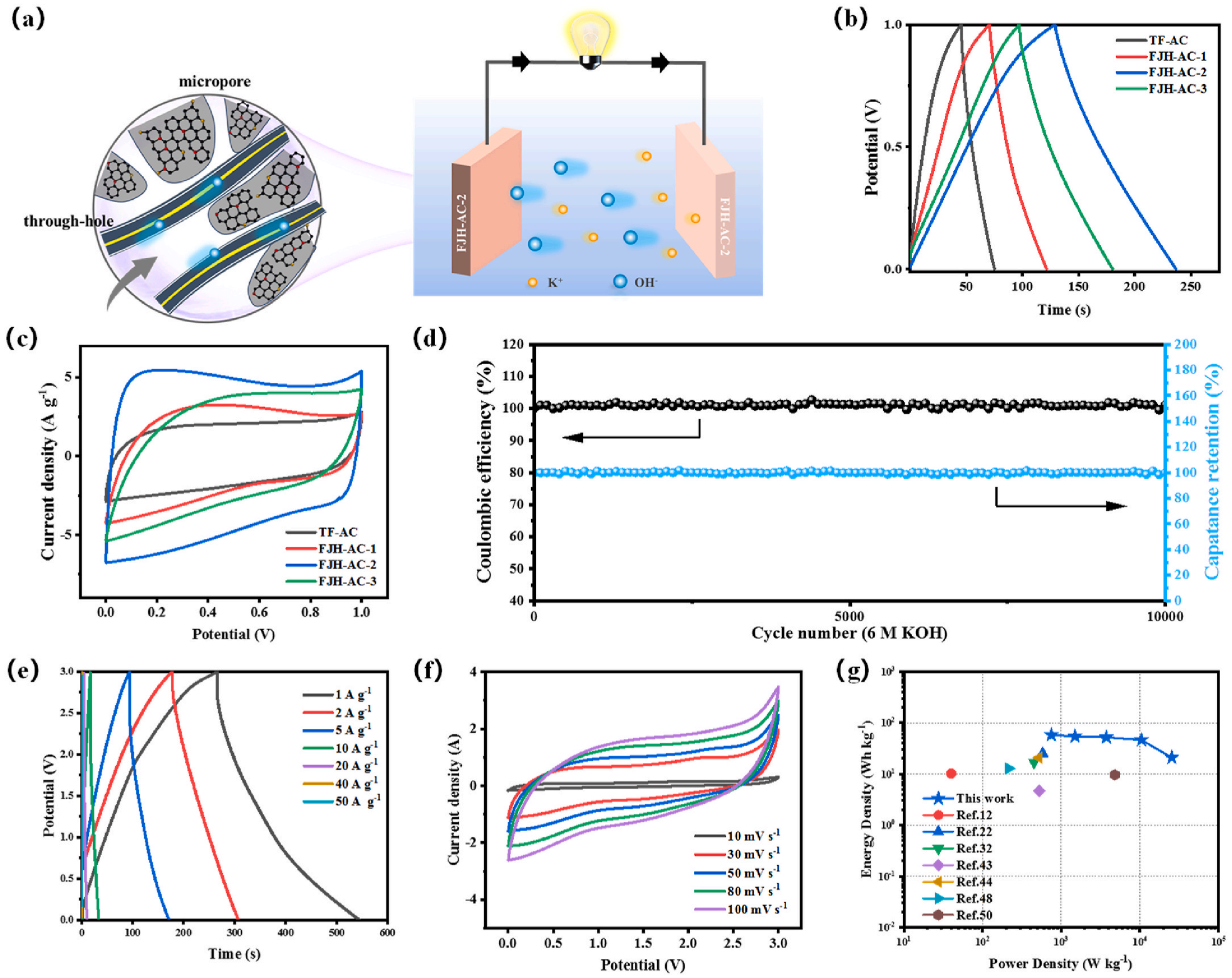

Fig. 4. Electrochemical performances of TF-AC and FJH-AC-X were tested in a two-electrode system in different electrolytes:(a) Schematic diagram of assembling supercapacitor in 6 M KOH electrolyte; (b) GCD curves for TF-AC and FJH-AC-X at 1 A g^{-1} and (c) CV curves measured at 50 mV s^{-1} in 6 M KOH electrolyte; (d) Cycling stability of FJH-AC-2 tested at 5 A g^{-1} in 6 M KOH; (e) GCD curves obtained at different current densities and (f) CV curves of FJH-AC-2 at different scan rates in 1 M TEATFB/AN electrolyte; (g) Ragone plots of FJH-AC-2 capacitors.

performance. The 10000 cycles test was carried out at 5 A g^{-1}, which showed that the electrode had a cycle retention rate of 99.84 % in 6 M KOH (Fig. 2d). It may be attributed to the structure of carbon material is relatively stable during the cycling [59]. The coulomb efficiency of FJH-AC-2 remains above 98 % after 10,000 cycles, demonstrating the exceptional stability. In order to further explore its application value, FJH-AC-2 was assembled into a button cell using TEATFB/AN as the electrolyte, and its electrochemical performance was investigated. From 4e and 4f, the voltage window range of the button cell is as high as 3 V, and the specific capacitance of FJH-AC-2 can reach 185.4 F g^{-1} at 1 A g^{-1}, connecting two button cells can make a small bulb shine (Video S1). Fig. 4g presents the Ragone diagram of FJH-AC-2 in 1 M TEATFB/AN electrolyte, which exhibits an energy density of 57.8 Wh kg^{-1} at a power density of 748.5 W kg^{-1}, as compared to other literature sources (Table S8).

4. Conclusion

The FJH has the advantages of short time and low energy consumption during the thermal treatment of AC compared to the classical heating method of a tubular furnace. The rapid reaction process results in the formation of a substantial number of ultra-micropores within the electrode material, retains interconnected pore channels, and prevents activating agent further etching of heteroatoms. Based on these advantages, the sample prepared by FJH method has richer pore structure and heteroatom content, the presence of ultra-micropores can significantly increase the specific capacitance, the interconnected pores provide ion transport channels, more N element content (3.32 %) can reduce the resistance and improve its conductivity, and the substantial presence of O element (24.18 %) can enhance the wettability. From this, the FJH-AC-2 has a higher specific capacitance of 313.7 F g^{-1} and achieves a power density of 748.5 W kg^{-1} at an energy density of 57.8 Wh kg^{-1} in 1 M TEATFB/AN electrolyte. This manuscript indicates that the coal-based porous carbon prepared by the FJH method requires a smaller quantity of activator than the traditional tube furnace, ensure better electrochemical performance while preparing quickly, and its yield can reach an astonishing 71.3 %. This provides a good strategy for the rapid preparation of coal-based porous carbon.

CRediT authorship contribution statement

Hongxia Gao: Writing – original draft. **Yikun Li:** Software. **Xueyan**

Wu: Writing – review & editing, Supervision. **Yan Lv:** Formal analysis. **Chunmei Ma:** Funding acquisition. **Yanchun Pei:** Writing – review & editing. **Na Liang:** Data curation. **Fanze Meng:** Software. **Pengfei Dong:** Formal analysis. **Jixi Guo:** Writing – review & editing, Funding acquisition.

Declaration of competing interest

The authors declare that they have no known competing financial interests or personal relationships that could have appeared to influence the work reported in this paper.

Acknowledgements

This work is supported by the Open Project of Key Laboratory in Xinjiang Uygur Autonomous Region of China (2023D04032), the National Natural Science Foundation of China (U2003307, 22105163), Science and Technology Innovation Leader of Xinjiang Uygur Autonomous Region of China (2022TSYCLJ0043), the Natural Science Foundation of Xinjiang Uygur Autonomous Region of China (2021D01D09), Excellent Doctoral Innovation Project of Xinjiang University (XJU2023BS041). Hami Oil-rich Coal Clean and Efficient Use Innovation Team (2024hmkjcxtd01).

Appendix A. Supplementary data

Supplementary data to this article can be found online at https://doi.org/10.1016/j.jpowsour.2025.237129.

Data availability

No data was used for the research described in the article.

References

[1] Y. Zou, C. Liu, L. Xu, Y. Li, M. Dong, W. Kong, B. Shen, Z. Wang, X. Wang, J. Yang, Synergistic effect of green trace K_2CO_3 and CO_2 activation of zhundong coal for high-performance supercapacitors, J. Power Sources 602 (2024) 234333, https://doi.org/10.1016/j.jpowsour.2024.234333.

[2] X. Liu, C.F. Liu, S. Xu, T. Cheng, S. Wang, W.Y. Lai, W. Huang, Porous organic polymers for high-performance supercapacitors, Chem. Soc. Rev. 51 (2022) 3181–3225, https://doi.org/10.1039/d2cs00065b.

[3] D. Wang, Y. Lian, H. Fu, Q. Zhou, Y. Zheng, H. Zhang, Flexible porous carbon nanofibers derived from cuttlefish ink as self-supporting electrodes for supercapacitors, J. Power Sources 599 (2024) 234216, https://doi.org/10.1016/j.jpowsour.2024.234216.

[4] Z. Luo, B. Kou, Y. Wang, Y. Song, M. Weng, C. Liu, W. Zhang, L. Chen, Toy-blocks-inspired programmable supercapacitors with high energy density, Chem. Eng. J. 445 (2022) 136788, https://doi.org/10.1016/j.cej.2022.136788.

[5] Q. Li, M. Liu, F. Huang, X. Zuo, X. Wei, S. Li, H. Zhang, Co_9S_8@MnO_2 core–shell defective heterostructure for high-voltage flexible supercapacitor and Zn-ion hybrid supercapacitor, Chem. Eng. J. 437 (2022) 135494, https://doi.org/10.1016/j.cej.2022.135494.

[6] L. Lai, J. Li, Y. Deng, Z. Yu, L. Wei, Y. Chen, Carbon and carbon/metal hybrid structures enabled by ultrafast heating methods, Small Struct 3 (2022) 11, https://doi.org/10.1002/sstr.202200112.

[7] J. Peng, X. Kang, S. Zhao, Y. Yin, P. Zhao, A.J. Ragauskas, C. Si, X. Song, Regulating the properties of activated carbon for supercapacitors: impact of particle size and degree of aromatization of hydrochar, Adv. Compos. Hybrid Mater. 6 (2023) 107, https://doi.org/10.1007/s42114-023-00682-9.

[8] J. Liang, Z. Wang, L. Huang, P. Zou, X. Liu, Q. Ni, X. Wang, W. Wang, R. Tao, Facile and tunable synthesis of nitrogen-doped graphene with different microstructures for high-performance supercapacitors, ACS Mater. Lett. 5 (2023) 944–954, https://doi.org/10.1021/acsmaterialslett.2c01092.

[9] T. Xu, Y. Wang, K. Liu, Q. Zhao, Q. Liang, M. Zhang, C. Si, Ultralight MXene/carbon nanotube composite aerogel for high-performance flexible supercapacitor, Adv. Compos. Hybrid Mater. 6 (2023) 108, https://doi.org/10.1007/s42114-023-00675-8.

[10] J.W. Graydon, M. Panjehshahi, D. Kirk, Charge redistribution and ionic mobility in the micropores of supercapacitors, J. Power Sources 245 (2014) 822–829, https://doi.org/10.1016/j.jpowsour.2013.07.036.

[11] H. Su, H. Zhang, F. Liu, F. Chun, B. Zhang, X. Chu, H. Huang, W. Deng, B. Gu, H. Zhang, X. Zheng, M. Zhu, W. Yang, High power supercapacitors based on hierarchically porous sheet-like nanocarbons with ionic liquid electrolytes, Chem. Eng. J. 322 (2017) 73–81, https://doi.org/10.1016/j.cej.2017.04.012.

[12] T. Zhao, D. Yang, B.X. Li, Y. Shi, Q. Quan, N. Koratkar, Z.Z. Yu, Supercapacitor architecture for extreme low-temperature operation featuring MXene/carbon nanotube electrodes with vertically aligned channels and a novel freeze-resistant electrolyte, Adv. Funct. Mater. 34 (2024) 2314825, https://doi.org/10.1002/adfm.202314825.

[13] P.Z. Yang, Dingyuan Zhu, Penghui Jiang, Feng Bi, Xiaotao, Biocarbon with large specific surface area and tunable pore structure from binary molten salt templating for supercapacitor applications, Chem. Eng. J. 472 (2023) 144785, https://doi.org/10.1016/j.cej.2023.144785.

[14] J. Yin, W. Zhang, N.A. Alhebshi, N. Salah, H.N. Alshareef, H. N. Synthesis strategies of porous carbon for supercapacitor applications, Small Methods 4 (2020) 1900853, https://doi.org/10.1002/smtd.201900853.

[15] S. Hou, W. Cheng, F. Guo, Fast joule-heating synthesized heteroatom-doped carbon and its impressive electrochemical performance, Sustain. Mater. Technol. 35 (2023) e00570, https://doi.org/10.1016/j.susmat.2023.e00570.

[16] S. Zhang, J. Zhu, Y. Qing, L. Wang, J. Zhao, J. Li, W. Tian, D. Jia, Z. Fan, Ultramicroporous carbons puzzled by graphene quantum dots: integrated high gravimetric, volumetric, and areal capacitances for supercapacitors, Adv. Funct. Mater. 28 (2018) 1805898, https://doi.org/10.1002/adfm.201805898.

[17] W. Li, W. Zhang, Y. Xu, G. Wang, W. Sui, T. Xu, Z. Yuan, C. Si, Heteroatom-doped lignin derived carbon materials with improved electrochemical performance for advanced supercapacitors, Chem. Eng. J. 497 (2024) 154829, https://doi.org/10.1016/j.cej.2024.154829.

[18] S. Roy, R. Samanta, S. Barman, Electrospun N-doped carbon-carbon nanofibers with enhanced porosity for high-performance zinc-ion hybrid supercapacitor application, Small Sci (2025) 2400426, https://doi.org/10.1002/smsc.202400426.

[19] D. Dong, Y. Zhang, Y. Xiao, T. Wang, J. Wang, W. Pan, Synthesis of O-doped coal-based carbon electrode materials by ultrasound-assisted bimetallic activation for application in supercapacitors, Appl. Surf. Sci. 529 (2020) 147074, https://doi.org/10.1016/j.apsusc.2020.147074.

[20] H. Pan, X. Jiao, W. Zhang, L. Fan, Z. Yuan, C. Zhang, Supercapacitor with ultra-high power and energy density enabled by nitrogen/oxygen-doped interconnected hollow carbon nano-onions, Chem. Eng. J. 484 (2024) 149663, https://doi.org/10.1016/j.cej.2024.149663.

[21] J. Wang, X. Li, K. Tian, W. Guo, B. Zhang, J. Zhang, M. Li, Z. Xing, X. Li, J. Xu, H. Wang, Highly accessible 3D interconnected macro/microporous catechol-enriched carbon material to clarify its excellent pseudocapacitance, ACS Mater. Lett. 6 (2024) 4571–4580, https://doi.org/10.1021/acsmaterialslett.4c01175.

[22] L. Deng, J. Shi, Y. Zhao, D. Feng, W. Zhang, Y. Yu, S. Sun, Straw-based biochar prepared from multi-step KOH activation and its structure-effect relationship of CO_2 capture under atmospheric/pressurized conditions via experimental analysis and MD/DFT calculations, Chem. Eng. J. 495 (2024) 153403, https://doi.org/10.1016/j.cej.2024.153403.

[23] X. Zhao, W. Jia, X. Wu, Y. Lv, J. Qiu, J. Guo, X. Wang, D. Jia, J. Yan, D. Wu, Ultrafine MoO_3 anchored in coal-based carbon nanofibers as anode for advanced lithium-ion batteries, Carbon 156 (2020) 445–452, https://doi.org/10.1016/j.carbon.2019.09.065.

[24] S. Lv, X. Wu, Y. Lv, Z. Wang, N. Liang, Y. Pei, A. Xuhrat, J. Guo, Super-hydrophilic coal-based carbon fibers as flexible electrodes for supercapacitors, Energy Fuels 37 (2023) 12427–12435, https://doi.org/10.1021/acs.energyfuels.3c01697.

[25] S. Ghosh, S. Barg, S.M. Jeong, K. Ostrikov, Heteroatom-doped and oxygen-functionalized nanocarbons for high-performance supercapacitors, Adv. Energy Mater. 10 (2020) 2001239, https://doi.org/10.1002/aenm.202001239.

[26] A. Deshpande, S. Rawat, I.M. Patil, S. Rane, T. Bhaskar, S.B. Ogale, S. Hotha, Converting renewable saccharides to heteroatom doped porous carbons as supercapacitor electrodes, Carbon 214 (2023) 118368, https://doi.org/10.1016/j.carbon.2023.118368.

[27] M. Cai, X. Wei, H. Huang, F. Yuan, C. Li, S. Xu, X. Liang, W. Zhou, J. Guo, Nitrogen-doped $Ti_3C_2T_x$ MXene prepared by thermal decomposition of ammonium salts and its application in flexible quasi-solid-state supercapacitor, Chem. Eng. J. 458 (2023) 118368, https://doi.org/10.1016/j.cej.2023.141338.

[28] Z. Liu, C. Duan, S. Dou, Q. Yuan, J. Xu, W.D. Liu, Y. Chen, Ultrafast porous carbon activation promises high-energy density supercapacitors, Small 18 (2022) e2200954, https://doi.org/10.1002/smll.202200954.

[29] Y. Chen, Y. Wang, Kun Fu, Valencia A. Danner, J. Dai, S.D. Lacey, Y. Yao, L. Hu, Rapid, in situ synthesis of high capacity battery anodes through high temperature radiation-based thermal shock, Nano Lett. 16 (2016) 5553–5558, https://doi.org/10.1021/acs.nanolett.6b02096.

[30] L. Hou, W. Yang, B. Jiang, P. Wang, L. Yan, C. Zhang, G. Huang, F. Yang, Y. Li, Intrinsic defect-rich porous carbon nanosheets synthesized from potassium citrate toward advanced supercapacitors and microwave absorption, Carbon 183 (2021) 176–186, https://doi.org/10.1016/j.carbon.2021.06.072.

[31] W. Liu, S. Zhang, S.U. Dar, Y. Zhao, R. Akram, X. Zhang, S. Jin, Z. Wu, D. Wu, Polyphosphazene-derived heteroatoms-doped carbon materials for supercapacitor electrodes, Carbon 129 (2018) 420–427, https://doi.org/10.1016/j.carbon.2017.12.016.

[32] J.Y.J. Cui, J. Meng, Y. Liu, M. Liao, T. Wu, M. Dresselhaus, Y. Xie, J. Wu, C. Lu, X. Zhang, Supermolecule cucurbituril subnanoporous carbon supercapacitor (SCSCS), Nano Lett. 21 (2021) 2156–2164, https://doi.org/10.1016/j.carbon.2017.12.016.

[33] X. Zhang, H. Li, B. Qin, Q. Wang, X. Xing, D. Yang, L.e. Jin, Q. Cao, Direct synthesis of porous graphitic carbon sheets grafted on carbon fibers for high-performance supercapacitors, J. Mater. Chem. A 7 (2019) 3298–3306, https://doi.org/10.1039/c8ta11844b.

[34] M. Wang, J. Yang, S. Liu, X. Che, S. He, G. Chen, J. Qiu, Nitrogen-doped porous carbon electrode for aqueous iodide redox supercapacitor, Chem. Eng. J. 451 (2023) 138501, https://doi.org/10.1016/j.cej.2022.138501.

[35] Y. Yang, Y. Liu, Y. Li, B. Deng, B. Yin, M. Yang, Design of compressible and elastic N-doped porous carbon nanofiber aerogels as binder-free supercapacitor electrodes, J. Mater. Chem. A 8 (2020) 17257–17265, https://doi.org/10.1039/d0ta05423b.

[36] L. Zheng, B. Tang, X. Dai, T. Xing, Y. Ouyang, Y. Wang, B. Chang, H. Shu, X. Wang, High-yield synthesis of N-rich polymer-derived porous carbon with nanorod-like structure and ultrahigh N-doped content for high-performance supercapacitors, Chem. Eng. J. 399 (2020) 125671, https://doi.org/10.1016/j.cej.2020.125671.

[37] N. Talreja, S. Jung, L.T.H. Yen, T. Kim, Phenol-formaldehyde-resin-based activated carbons with controlled pore size distribution for high-performance supercapacitors, Chem. Eng. J. 379 (2020) 122332, https://doi.org/10.1016/j.cej.2019.122332.

[38] A.R. Panneer Selvam, S. Pandiyarajan, A.-H. Liao, S.S.M. Manickaraj, G. Baskaran, M. Selvaraj, M.A. Assiri, H. Zhou, H.-C. Chuang, Phase-controlled preparation of cubic facet zeolitic imidazole framework-8-derived carbon using supercritical-CO_2 medium: a solitary carbon material for symmetric supercapacitor, Carbon 222 (2024) 118968, https://doi.org/10.1016/j.carbon.2024.118968.

[39] T. Mo, J. Peng, W. Dai, M. Chen, V. Presser, G. Feng, Horn-like pore entrance boosts charging dynamics and charge storage of nanoporous supercapacitors, ACS Nano 17 (2023) 14974–14980, https://doi.org/10.1021/acsnano.3c03886.

[40] F. Le, P. Ren, W. Jia, T. Wang, Y. Tao, D. Wu, High-yield preparation of coal tar pitch based porous carbon via low melting point fire retardant carbonation strategy for supercapacitor, Chem. Eng. J. 470 (2023) 144131, https://doi.org/10.1016/j.cej.2023.144131.

[41] G.Y.J. Chmiola, Y. Gogotsi, C. Portet, P. Simon, P.L. Taberna, Taberna, Anomalous increase in carbon capacitance at pore sizes less than 1 nanometer, Science 313 (2006) 22, https://doi.org/10.1126/science.1132195.

[42] J. Chmiola, C. Largeot, P.L. Taberna, P. Simon, Y. Gogotsi, Desolvation of ions in subnanometer pores and its effect on capacitance and double-layer theory, Angew. Chem. Int. Ed. 47 (2008) 3392–3395, https://doi.org/10.1002/anie.200704894.

[43] L. Pu, J. Zhang, N.K.L. Jiresse, Y. Gao, H. Zhou, N. Naik, P. Gao, Z. Guo, N-doped MXene derived from chitosan for the highly effective electrochemical properties as supercapacitor, Adv. Compos. Hybrid Mater. 5 (2021) 356–369, https://doi.org/10.1007/s42114-021-00371-5.

[44] G. Pan, F. Cao, Y. Zhang, X. Xia, N-doped carbon nanofibers arrays as advanced electrodes for supercapacitors, J. Mater. Sci. Technol. 55 (2020) 144–151, https://doi.org/10.1016/j.jmst.2019.10.00.

[45] J. Du, Y. Zhang, H. Wu, S. Hou, A. Chen, N-doped hollow mesoporous carbon spheres by improved dissolution-capture for supercapacitors, Carbon 156 (2020) 523–528, https://doi.org/10.1016/j.carbon.2019.09.091.

[46] B. Guo, R. Ma, Z. Li, S. Guo, J. Luo, M. Yang, Q. Liu, T. Thomas, J. Wang, Hierarchical N-doped porous carbons for Zn-air batteries and supercapacitors, Nano-Micro Lett. 12 (2020) 20, https://doi.org/10.1007/s40820-019-0364-z.

[47] L. Ni, R. Wang, H. Wang, C. Sun, B. Sun, X. Guo, S. Jiang, Z. Shi, W. Jing, L. Zhu, S. Qiu, Z. Zhang, Designing nanographitic domains in N-doped porous carbon foam for high performance supercapacitors, Carbon 139 (2018) 1152–1159, https://doi.org/10.1016/j.carbon.2018.07.057.

[48] J. Li, K. Han, D. Wang, Z. Teng, Y. Cao, J. Qi, M. Li, M. Wang, Fabrication of high performance structural N-doped hierarchical porous carbon for supercapacitors, Carbon 164 (2020) 42–50, https://doi.org/10.1016/j.carbon.2020.03.044.

[49] C. Xia, S. Surendran, S. Ji, D. Kim, Y. Chae, J. Kim, M. Je, M. Han, W. Choe, C. H. Choi, H. Choi, J.K. Kim, U. Sim, Heteroatom tuning in agarose derived carbon aerogel for enhanced potassium ion multiple energy storage, Carbon Energy 4 (2022) 491–505, https://doi.org/10.1002/cey2.427.

[50] M. Cao, Y. Feng, R. Tian, Q. Chen, J. Chen, M. Jia, J. Yao, Modification of the surface chemistry of activated carbons, Carbon 161 (2020) 224–230, https://doi.org/10.1016/j.carbon.2020.01.093.

[51] A. Wang, K. Sun, R. Xu, Y. Sun, J. Jiang, Cleanly synthesizing rotten potato-based activated carbon for supercapacitor by self-catalytic activation, J. Clean. Prod. 283 (2021) 125385, https://doi.org/10.1016/j.jclepro.2020.125385.

[52] Y. Yao, R. Zhou, Y. Yu, J. Chen, C. Du, Y. Zhang, T. Long, L. Wan, Q. Wang, M. Xie, Solvent-freely polymerizing catechol and paraformaldehyde to nitrogen-rich carbon for high-volumetric-performance supercapacitor, Chem. Eng. J. 472 (2023) 144905, https://doi.org/10.1016/j.cej.2023.144905.

[53] R. Dupuis, P.L. Valdenaire, R.J. Pellenq, K. Ioannidou, How chemical defects influence the charging of nanoporous carbon supercapacitors, Proc. Natl. Acad. Sci. USA. 119 (2022) e2121945119.

[54] T. Lv, X. Yang, Y. Zhang, X. Wang, J. Qiu, Fabrication of soft-hard heterostructure porous carbon with enhanced performance for high mass-loading aqueous supercapacitors, Small 2310645 (2024) 1–13, https://doi.org/10.1002/smll.202310645.

[55] W. Zhang, W. Li, S. Li, Molten salt assisted self-activated carbon with controllable architecture for aqueous supercapacitor, J. Mate. Sci. Technol. 156 (2023) 107–117, https://doi.org/10.1016/j.jmst.2022.12.079.

[56] B. Chen, D. Wu, T. Wang, F. Yuan, D. Jia, Rapid preparation of porous carbon by flame burning carbonization method for supercapacitor, Chem. Eng. J. 462 (2023) 142163, https://doi.org/10.1016/j.cej.2023.142163.

[57] C. Liu, L. Wang, Z. Xia, R. Chen, H.-L. Wang, Y. Liu, Carbon hollow fibers with tunable hierarchical structure as self-standing supercapacitor electrode, Chem. Eng. J. 431 (2022) 134099, https://doi.org/10.1016/j.cej.2021.134099.

[58] J. Zhu, Q. Zhang, Y. Zhao, R. Zhang, L. Liu, J. Yu, Robust N-doping porous carbon nanofiber membranes with inter-fiber cross-linked structures for supercapacitors, Carbon 202 (2023) 13–25, https://doi.org/10.1016/j.carbon.2022.11.021.

[59] G. Han, J. Jia, Q. Liu, G. Huang, B. Xing, C. Zhang, Y. Cao, Template-activated bifunctional soluble salt $ZnCl_2$ assisted synthesis of coal-based hierarchical porous carbon for high-performance supercapacitors, Carbon 186 (2022) 380–390, https://doi.org/10.1016/j.carbon.2021.10.042.